Searching for new solar twins: The 𝕀𝕟𝕥𝕚 survey for the Northern Sky

Jhon Yana Galarza [1]⋆ Ricardo López-Valdivia [2]⋆ Diego Lorenzo-Oliveira [1]⋆ Henrique Reggiani [3]
Jorge Meléndez [1] Daniel Gamarra-Sánchez [4] Matias Flores [5,6,7] Jerry Portal-Rivera [4]
Paula Miquelarena [5,6,7] Geisa Ponte [1,8] Kevin C. Schlaufman [3] and Teófilo Vargas Auccalla [4]

[1] *Universidade de São Paulo, Departamento de Astronomia do IAG/USP, Rua do Matão 1226 Cidade Universitária, 05508-900 São Paulo, SP, Brazil*
[2] *Department of Astronomy, The University of Texas at Austin, 2515 Speedway, Stop C1400, Austin, TX 78712-1205, USA*
[3] *Department of Physics and Astronomy, Johns Hopkins University, 3400 N Charles St., Baltimore, MD 21218, USA*
[4] *Seminario Permanente de Astronomía y Ciencias Espaciales, Facultad de Ciencias Físicas, Universidad Nacional Mayor de San Marcos, Avenida Venezuela s/n, Lima 15081, Perú*
[5] *Facultad de Ciencias Exactas, Físicas y Naturales, Universidad Nacional de San Juan, J5402DCS San Juan, Argentina*
[6] *Consejo Nacional de Investigaciones Científicas y Técnicas (CONICET), C1425FQB, Argentina*
[7] *Instituto de Ciencias Astronómicas, de la Tierra y del Espacio (ICATE), España Sur 1512, CC 49, 5400 San Juan, Argentina*
[8] *CRAAM, Mackenzie Presbyterian University, Rua da Consolação, 896 São Paulo, SP, Brazil*

ABSTRACT
Solar twins are key in different areas of astrophysics, however only just over a hundred were identified and well-studied in the last two decades. In this work, we take advantage of the very precise *Gaia* (DR2/EDR3), Tycho, and 2MASS photometric systems to create the 𝕀𝕟𝕥𝕚 survey of new solar twins in the Northern Hemisphere. The spectra of our targets were initially obtained with spectrographs of moderate resolution (ARCES and Goodman spectrographs with $R = 31\,500$ and $11\,930$, respectively) to find the best solar twin candidates and then observed at McDonald Observatory with higher resolving power (TS23, $R = 60\,000$) and signal-to-noise ratio (SNR ~ 300–500). The stellar parameters were estimated through the differential spectroscopic equilibrium relative to the Sun, which allow us to achieve a high internal precision ($\sigma(T_{\rm eff}) = 15\,{\rm K}$, $\sigma(\log g) = 0.03\,{\rm dex}$, $\sigma({\rm [Fe/H]}) = 0.01\,{\rm dex}$, and $\sigma(v_t) = 0.03\,{\rm km\,s^{-1}}$). We propose a new class of stars with evolution similar to the Sun: solar proxy, which is useful to perform studies related to the evolution of the Sun, such as its rotational and magnetic evolution. Its definition is based on metallicity ($-0.15\,{\rm dex} \leq {\rm [Fe/H]} \leq +0.15\,{\rm dex}$) and mass ($0.95\,{\rm M_\odot} \leq M \leq 1.05\,{\rm M_\odot}$) constraints, thus assuring that the star follows a similar evolutionary path as the Sun along the main sequence. Based on this new definition, we report 70 newly identified solar proxies, 46 solar analogues, and 13 solar-type stars. In addition, we identified nine close solar twins whose stellar parameters are the most similar to those of the Sun.

Key words: techniques: spectroscopic – stars: abundances – stars: activity – stars: atmospheres – stars: fundamental parameters – stars: solar-type.

1 INTRODUCTION

Since the 1980s, the astronomical community was interested in finding stars with physical parameters similar to those of the Sun, i.e. solar twins. However, a crucial question arose: which parameters should be considered to define an object as solar twin?. Cayrel de Strobel et al. (1981), Cayrel de Strobel & Bentolila (1989), Cayrel de Strobel (1996) defined these objects as stars whose effective temperature ($T_{\rm eff}$), surface gravity ($\log g$), metallicity ([Fe/H]), microturbulence (v_t), photometric properties, chemical composition, age, luminosity, rotation, and magnetic fields are similar, if not identical, to those of the Sun. These authors performed the first attempts to find real solar twins exploiting a list of 78 solar analogues obtained by Hardorp (1978) through spectrophotometric observations. However, with these constraints, it was almost impossible to find a real solar twin. A less rigorous definition was carried out by Friel et al. (1993): 'every observable and derivable physical quantity must be identical within observational errors to that of the Sun'. Porto de Mello & da Silva (1997), using the Cayrel de Strobel's definition (Cayrel de Strobel & Bentolila 1989), were able to find the first closest solar twin: 18 Sco. Years later, other authors also claimed to have identified solar twins based on photometric and spectroscopic parameters constraints: HD 143436 (King, Boesgaard & Schuler 2005), HD 98618 (Meléndez, Dodds-Eden & Robles 2006), HD 10307 and HD 34411 (Galeev et al. 2004), and finally HD 101364 and HD 133600 (Meléndez & Ramírez 2007), the latter ones not only reproduce the solar fundamental parameters but also a low lithium abundance. On the other hand, Ramírez, Meléndez & Asplund (2009) introduced a concept of solar twin based only on spectroscopic stellar parameters constraints (i.e. only $T_{\rm eff}$, $\log g$, and [Fe/H]), which is useful for achieving high precision differential abundances relative to the Sun; however, this definition introduces a slight bias in the mass–age–[Fe/H] space that will be discussed later. One of the last definitions comes from Datson, Flynn & Portinari (2012, 2014, 2015), where

⋆ E-mail: ramstojh@usp.br (JYG); rlopezv@utexas.edu (RL-V); diegolorenzo@usp.br (DL-O)

a solar twin is defined as a star whose stellar parameters (estimated only with high resolution spectrographs) are indistinguishable from solar within the errors. A very comprehensive discussion about the concept of solar twins and solar analogues is given in Porto de Mello et al. (2014). These authors suggest that solar twins should not be only indistinguishably from the Sun, but also follow a similar evolutionary history. In brief, the literature is full of different definitions of solar twins, but until now it is not yet clear which parameters should define a real solar twin, thus hindering the efforts for finding these objects as well as studies such as gyrochronology and magnetic activity evolution (e.g. Lorenzo-Oliveira et al. 2018).

To date, despite different definitions in the literature, approximately 100 solar twins have been identified by different authors (e.g. Pasquini et al. 2008; Meléndez et al. 2009, 2014a; Ramírez et al. 2009; Takeda & Tajitsu 2009; Baumann et al. 2010; González Hernández et al. 2010; Önehag et al. 2011; Sousa et al. 2011; Datson et al. 2012; do Nascimento et al. 2013; Porto de Mello et al. 2014; Ramírez et al. 2014; Galarza, Meléndez & Cohen 2016; Giribaldi et al. 2019) and their applications in different astrophysical fields have had significant impacts on our knowledge about stars and the Sun. For example, they are useful for setting the zero-point of fundamental photometric calibrations (Holmberg, Flynn & Portinari 2006; Casagrande et al. 2010; Ramírez et al. 2012; Datson et al. 2014; Casagrande et al. 2020), studying the mineralogy of asteroids by subtracting the Sun's reflected light on them (e.g. Lazzaro et al. 2004; Jasmim et al. 2013), testing stellar interiors through asteroseismology (Chaplin et al. 2011; Bazot et al. 2012, 2018), measuring distances (Jofré et al. 2015), and even improving spectroscopic methods for stellar parameters determination (Saffe et al. 2018). More recently, Yana Galarza et al. (2021) detected for the first time a differential odd–even effect relative to the Sun in the solar twin HIP 11915, providing new insights to understand the supernova nucleosynthesis history.

The study of solar twins has also contributed to the understanding of the chemical evolution of the Galactic disc (da Silva et al. 2012; Nissen 2015; Spina et al. 2016b, 2018; Bedell et al. 2018; Botelho et al. 2020; Nissen et al. 2020), and the study of the neutron-capture elements (Meléndez et al. 2014b; Yana Galarza et al. 2016). As a result, new chemical clocks as the [Y/Mg]–age correlation initially proposed by da Silva et al. (2012) and improved by several authors (e.g. Nissen 2015; Tucci Maia et al. 2016; Feltzing et al. 2017; Spina et al. 2018; Jofré, Jackson & Tucci Maia 2020; Nissen et al. 2020) and the Li–age correlation (Baumann et al. 2010; Carlos, Nissen & Meléndez 2016; Carlos et al. 2019) have been established. Biology principles (Phylogenetics of solar twins) have also been applied to investigate the chemical evolution of the Milky Way (Jofré et al. 2017; Jackson et al. 2020).

Significant contributions come from the works of do Nascimento et al. (2013, 2020) and Lorenzo-Oliveira et al. (2019, 2020) in the field of gyrochronology using solar twins, giving important clues to understand the rotational evolution of the Sun. A controversial diagnostic of stellar ages is the age–chromospheric activity relation (Mamajek & Hillenbrand 2008; Pace 2013), whose applicability is extended for stars with ∼6–7 Gyr (Lorenzo-Oliveira, Porto de Mello & Schiavon 2016). Besides, the analysis of solar twins could help us to place the ∼11 yr solar cycle in context (Hall, Lockwood & Skiff 2007; Hall et al. 2009; Flores et al. 2018). Meléndez et al. (2009) reported chemical anomalies in the Sun when it is compared to solar twins, thereby establishing the basis for studying the planet–stellar chemical composition connection (e.g. Ramírez et al. 2009; González Hernández et al. 2010, 2013; Schuler et al. 2011; Adibekyan et al. 2014; Maldonado et al. 2015; Nissen 2015; Liu et al. 2016; Spina

et al. 2016b; Nissen et al. 2017; Bedell et al. 2018; Maia et al. 2019; Cowley, Bord & Yüce 2020). Finally, the study of solar twins is also expanded to the field of exoplanets. For instance, Bedell et al. (2015, 2017) and Meléndez et al. (2017) have demonstrated that with the high precision achieved in stellar parameters in solar twins, it is possible to get very precise exoplanet properties (mass and radius). Additionally, it is also feasible to study habitability and evolution of exoplanets through radioactive elements such as thorium (e.g. Unterborn, Johnson & Panero 2015; Botelho et al. 2019).

As widely discussed above, the identification of new solar twins is essential to the advancement of diverse astronomical fields. Therefore, in this work we present the ꟼnti[1] catalogue of new solar twins, solar analogues, and solar-type stars identified in the Northern Hemisphere. The ꟼnti survey provides reliable and precise spectroscopic stellar parameters, chromospheric activity levels, and photometric rotational periods when its determinations through high-precision light curves are possible.

2 SAMPLE SELECTION

Inspired by seminal works for searching solar twins (e.g. Hardorp 1978; Cayrel de Strobel et al. 1981; Meléndez & Ramírez 2007; Ramírez et al. 2009; Porto de Mello et al. 2014), in this era of large surveys, we take advantage of the precise photometric systems of *Gaia* DR2/EDR3 (Gaia Collaboration 2018, 2020), Tycho (Høg et al. 2000), and 2MASS (Skrutskie et al. 2006) to search these stellar objects. However, unlike these initial studies mainly based on photometric comparisons with the Sun, our methodology consist in performing colour constraints from the well characterized solar twins of Ramírez et al. (2014). To do so, we cross-matched the solar twin sample with the TGAS (Tycho-Gaia Astrometric Solution; Marrese et al. 2017) catalogue updated with the *Gaia* EDR3 magnitudes, resulting in 63 common objects. In our study, we also found a simple photometric relationship from *Gaia* EDR3 G (updated from our initial relations using DR2) to Tycho V and Johnson V (Kharchenko 2001):

$$V_{TG} = G \times 0.9942(\pm 0.0021) + 0.2657(\pm 0.0156) \qquad (1)$$

$$V_G = G \times 0.9940(\pm 0.0014) + 0.1929(\pm 0.0097), \qquad (2)$$

where V_{TG} is the transformation between G and Tycho V, while V_G is the conversion between G and Johnson V (see Fig. 1). The dispersion and the reduced chi-squared (χ^2_{red}) of the linear fit are 0.018 mag and 1.608 for equation (1), and 0.014 mag and 1.554 for equation (2), respectively. It is important to highlight that these relationships are valid only for solar twins.[2] Besides, V_{TG} is used only to establish the colour constraints showed in Table 1, while V_G is useful to estimate isochronal ages as it will be discussed later. In this way, we established the bounds of our colour constraints, which are shown in Table 1.

The sample selection technique consists in first cross-matching the *Gaia* DR2 (updated to EDR3 in Table 1) with the 2MASS and Tycho catalogues within a region of 100 pc from Earth and with G values ranging from 5 to 9 mag. Then, we applied our colour constraints in the cross-matched sample and found 3100 objects. These objects compose our preliminary sample of solar twin candidates and are plotted as red circles in the *Gaia* EDR3

---

[1] ꟼnti means Sun in the Inca–Andean–Quechua cosmovision.

[2] A similar relationship was found between *Gaia* DR2 G and Johnson V: $V_G = G \times 0.9901(\pm 0.0014) + 0.2346(\pm 0.0097)$
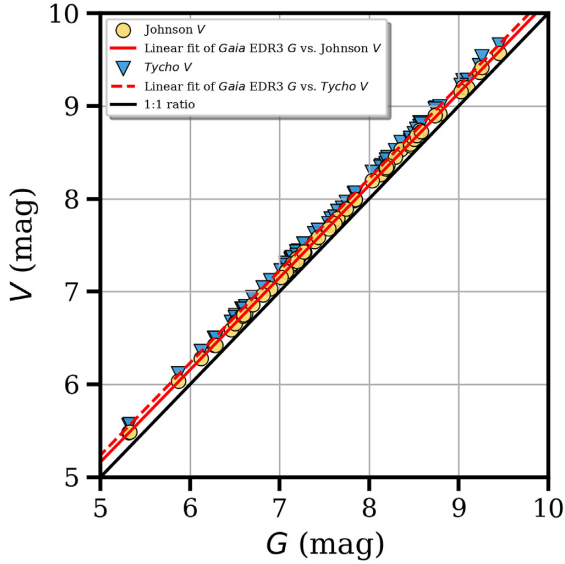
Figure 1. Photometric relationship between Johnson/Tycho *V* versus *Gaia* EDR3 *G* magnitudes, which are valid only for solar twins. Both the red line and the red dashed lines represent the linear fit to the data considering errors in both axis, while the black line is the 1:1 relation. Error bars are smaller than the symbols.

Table 1. *Gaia* absolute magnitude (M_G) and photometric colour constraints established using known solar twins (Ramírez et al. 2014). V_{TG} is the *V* magnitude based on equation (1), while B_T represent the Tycho *B* magnitude, G_{BP} and G_{RP} are *Gaia* EDR3 magnitudes in the BP and RP passbands, and *J*, *H*, K_S are 2MASS magnitudes.

Gaia absolute magnitude and colour constraints
$3.755 \leq M_G \leq 5.331$
$0.254 \leq G_{BP} - G \leq 0.377$
$0.455 \leq G - G_{RP} \leq 0.589$
$0.761 \leq G_{BP} - G_{RP} \leq 0.907$
$0.960 \leq G - J \leq 1.315$
$1.207 \leq G - H \leq 1.708$
$1.284 \leq G - K_S \leq 1.791$
$0.166 \leq J - H \leq 0.506$
$0.281 \leq J - K_S \leq 0.550$
$-0.002 \leq H - K_S \leq 0.180$
$0.473 \leq B_T - V_{TG} \leq 0.947$

Hertzsprung–Russell diagram[3] of Fig. 2. We did not apply reddening corrections for our sample, since it is within 100 pc and thus has negligible reddening. This is supported by Vergely et al. (2010) and Lallement et al. (2014), who found a gradient of d$E(B - V)$/dr = 0.0002 mag per pc (see fig. 2 in Lallement et al. 2014). A similar result is found by Green et al. (2019), who created a precise dust map using the Pan-STARRS1, 2MASS, and *Gaia* DR2 (including its parallaxes) photometric bands. On the other hand, Reis et al. (2011) reported interstellar absorption ($E(B - V) > 0.056$) in the local bubble for regions on the Galactic plane ($d > 60$ pc) with latitudes from $l \geq 270°$ up to $l \leq 45°$. However, the stars of the ʃᶰᵗⁱ survey that fall in this region have $d < 50$ pc and thus $E(B - V) = 0$.

Finally, as our photometric methodology (see Table 1) for searching solar twins is based only on stellar parameter constraints (Ramírez
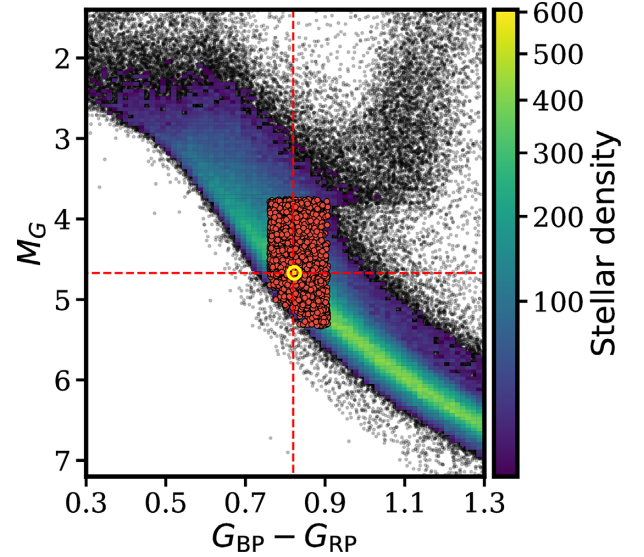

Figure 2. *Gaia* EDR3 HR diagram of ∼1.4 million stars within 200 pc from the Solar System (the data were obtained using the ASTROQUERY package). The colourmap represents the stellar density distribution created from the 2D histogram function of the matplotlib library. The red circles are the solar twin candidates found after applying our colour constraints. The Sun is plotted as a yellow solar standard symbol.

et al. 2009), it is expected to have a bias in our results (see the irregular polygon in Fig. 2), as our criteria are not symmetric relative to the main sequence evolution of a one-solar-mass solar-metallicity star. This will be discussed more extensively in subsection 4.2.

3 SPECTROSCOPIC OBSERVATIONS AND DATA REDUCTION

We obtained spectra of high signal-to-noise ratio (SNR ∼400) of our candidates with the Goodman High Throughput Spectrograph (Clemens, Crain & Anderson 2004), on the SOAR Telescope. From these spectra, we could retrieve a reliable initial guess of the spectroscopic parameters. The methodology consists in estimating [Fe/H] through spectral synthesis with the SP_ACE spectral analysis tool,[4] T_{eff} by using the colour–temperature–metallicity calibrations established by Casagrande et al. (2010), and trigonometric log g from *Gaia* EDR3 parallaxes with bolometric corrections given in Meléndez et al. (2006). Our technique was tested using several known solar twins and the results are consistent (within the uncertainties) with those estimated with high precision spectra (e.g. Spina et al. 2018). We also used the ARC Echelle Spectrograph (ARCES) on the 3.5-m Apache Point Observatory telescope to explore the northern sky since the observations with the SOAR telescope are inaccessible to DEC $\gtrsim +25°$. Thanks to these initial observations, we created a sample of 150 objects with the best solar twin candidates which were later observed with the Robert G. Tull Coudé Spectrograph (hereafter TS23; Tull et al. 1995) on the McDonald Observatory. The number of stars observed with each instrument and the internal precision achieved in stellar parameters are summarized in Table 2. In the following are detailed the spectroscopic observations performed in each observatory.

---

[3]Our HR diagram is based on https://vlas.dev/post/gaia-dr2-hrd/

[4]http://dc.g-vo.org/SP_ACE

Table 2. Number of stars observed with each instrument and the internal precision achieved in stellar parameters. (⋆) Number of stars observed in the Northern Hemisphere with $-18° \leq$ DEC $\leq +25°$.

Instrument	Observed stars	$\sigma(T_{\mathrm{eff}})$ (K)	$\sigma(\log g)$ (dex)	$\sigma([\mathrm{Fe/H}])$ (dex)
Goodman	160⋆	190	0.20	0.15
ARCES	20	100	0.11	0.08
TS23	147	15	0.03	0.01

3.1 SOAR telescope at Cerro Pachon

The spectra of the first potential solar twin candidates were obtained using the Goodman spectrograph on the 4.1-m SOAR Telescope under the programs SO2017B-004, SO2018A-005, SO2019A-007, and SO2019B-005 from 2017 to 2019. The solar spectrum was obtained after a short exposure of the Moon. The instrument was configured to use the red camera and the grating of 2100 lines per mm, resulting in a moderate resolving power $R = \lambda/\Delta\lambda = 12\,000$ and wavelength coverage of 630 Å centred at Hα. The Goodman spectra were reduced using IRAF[5] following the standard procedure, i.e. creation of the master flat, flat-field correction, sky subtraction, order extraction, etc. The radial velocity correction was performed using the `rvidlines` and `dopcor` task of IRAF. The obtained spectra were also normalized using IRAF's `continuum` task with orders ranging from two to five.

3.2 Apache point observatory

We also obtained the spectra of the solar twin candidates using the ARCES on the 3.5-m telescope at the Apache Point Observatory. The observations were carried out from 2019 to 2020. The solar spectra were obtained by observing the sky at twilight time. We used the CERES[6] pipeline in order to perform the standard reduction of the ARCES spectra. The ARCES spectrograph provides spectra of $R \sim 31\,500$ and covers the entire visible wavelength (from 3200–10 000 Å). The SNR achieved ranges from 200 to 300 at $\sim$6000 Å.

3.3 McDonald observatory

All the observations were taken during the years of 2018–2020 using the TS23 configured in its high resolution mode on the 2.7-m Harlan J. Smith Telescope at McDonald Observatory. The spectra of the Sun were obtained through the reflected light from the Moon. As the McDonald Observatory does not have an official pipeline to reduce the TS23 spectra, we have developed our own scripts[7] based on the practical reduction notes of the Dr. Chris Sneeden, Dr. Ivan Ramírez, and Dr. Diego Lorenzo-Oliveira. The code consists of a number of semi-automatic PYTHON scripts that performs bias subtraction, flat fielding, order extraction, and wavelength calibration using PYRAF (Science Software Branch at STScI 2012). The resulting spectra are free of fringing defects and have $R = 60\,000$, SNR $\sim$300–500 at $\sim$6500 Å, and cover a wide spectral range (from 3750–9900 Å).

---

[5] IRAF is distributed by the National Optical Astronomy Observatory, which is operated by the Association of the Universities for Research in Astronomy, Inc. (AURA) under cooperative agreement with the National Science Foundation.
[6] https://github.com/rabrahm/ceres
[7] https://github.com/ramstojh

4 FUNDAMENTAL PARAMETERS

4.1 Equivalent widths and stellar parameters

In order to perform the standard treatment and analysis of the TS23 spectra, we have developed semi-automatic PYTHON scripts[7], whose structure is a combination of two tools: ISPEC[8] and IRAF. In summary, the scripts use the ISPEC tool to perform the radial/barycentric velocity correction, and the `continuum` and `scombine` tasks of IRAF to normalize and combine the TS23 spectra. All the processes mentioned above are automatic resulting in spectra of high quality and SNR ($\sim$300–500 at 6500 Å). The scripts are also capable of measuring Equivalent Widths (EWs) through Gaussian fits to the line profile using the KAPTEYN `kmpfit` Package[9] in windows of 6 Å; however, this process is manually performed in order to achieve a higher precision. The method is based on line-by-line equivalent width measurements between the Sun and the object of interest, choosing consistent pseudo-continuum regions for both objects (e.g. Meléndez et al. 2009; Bedell et al. 2014; Yana Galarza et al. 2016; Spina et al. 2018). Besides, the script generates an output file containing information about the local continuum, limits of the Gaussian fits, χ^2 test, excitation potential, oscillator strength, and laboratory $\log(gf)$ values (see Meléndez et al. 2014b). On the other hand, as the ARCES spectra are already corrected by radial velocity shifts, we used our python scripts only to measure the EWs, rigorously following the same procedure already explained above.

As in our previous works (e.g. Ramírez et al. 2014; Yana Galarza et al. 2019), we employed the automatic q^2 (qoyllur-quipu)[10] python code to determine the spectroscopic stellar parameters (T_{eff}, $\log g$, [Fe/H], v_t) for our sample. In short, the code estimates the iron abundances using the line list from Meléndez et al. (2014b) and the 2019 version of the local thermodynamic equilibrium (LTE) code MOOG (Sneden 1973) with the Kurucz ODFNEW model atmospheres (Castelli & Kurucz 2003). Then, the q^2 employs the spectroscopic equilibrium, which is a standard technique of iron line excitation and ionization equilibrium. As a result, we obtain very reliable stellar parameters with high internal precision $\sigma(T_{\mathrm{eff}}) = 15$ K, $\sigma(\log g) = 0.03$ dex, $\sigma([\mathrm{Fe/H}]) = 0.01$ dex, and $\sigma(v_t) = 0.03$ km s^{-1}. The masses were inferred from an isochrone analysis, which is described in detail in subsection 4.3. Our inferred stellar parameters can be found in Table A1. In order to test the precision of the scripts and the reliability of the results, we compared our stellar parameters with those from Ramírez et al. (2013, 2014) and Spina et al. (2016a, 2018). As shown in Fig. 3, there is a good agreement between our results and those obtained using spectrographs of even higher resolution (e.g. HARPS spectrograph with $R \sim 115\,000$ in Spina et al. 2018) than the TS23.

4.2 New solar twins

As discussed earlier, the concept of solar twins changed over time (e.g. Cayrel de Strobel et al. 1981; Friel et al. 1993; Datson et al. 2012; Ramírez et al. 2014), and most of them are generally based on photometric and spectroscopic stellar parameters constraints but not on fundamental parameters that drive evolutionary states. The lack of the latter introduces a bias in the mass of the known solar twins, i.e. most of them are slightly more massive (~ 0.03 M$_\odot$) than the Sun (Ramírez et al. 2014; Spina et al. 2018). Thus, hampering the sample

---

[8] https://www.blancocuaresma.com/s/iSpec
[9] https://www.astro.rug.nl/software/kapteyn/
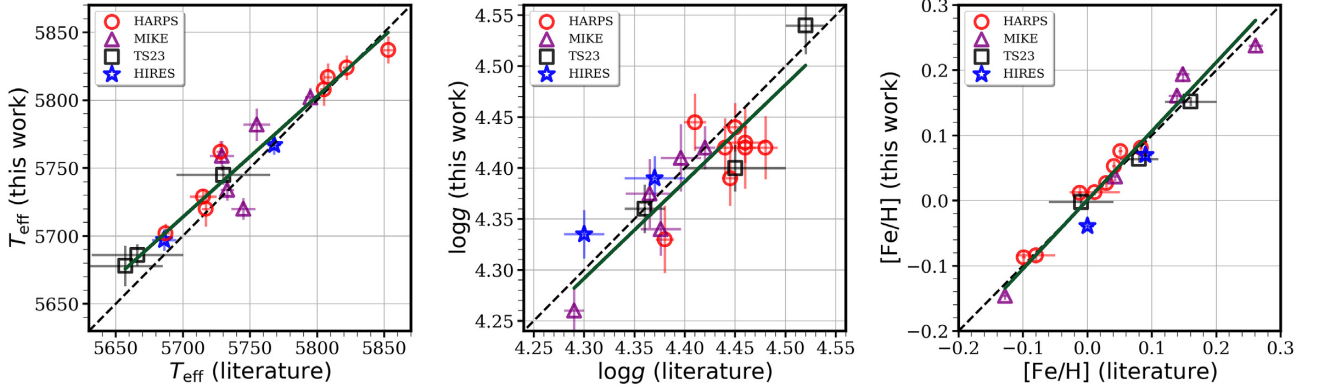[10] https://github.com/astroChasqui/q2

Figure 3. Comparison between our stellar parameters and those obtained by Ramírez, Allende Prieto & Lambert (2013), Ramírez et al. (2014) (squares and triangles) and Spina, Meléndez & Ramírez (2016a), Spina et al. (2018) (stars and circles). The dashed lines represent the 1:1 ratio, while the green lines are the linear fits for T_{eff} (left-hand panel, rms = 12 K), $\log g$ (middle panel, rms = 0.03 dex), and [Fe/H] (right-hand panel, rms = 0.02 dex).

selection for studies such as gyrochronology and magnetic activity evolution (e.g. Lorenzo-Oliveira et al. 2018, 2019). It is expected that our sample also has the same bias because we used the stellar parameters constraints given by Ramírez et al. (2014) (i.e. all stars with stellar parameters into $T_{eff} = 5777 \pm 100$ K, $\log g = 4.44 \pm 0.10$ dex, [Fe/H] $= 0.00 \pm 0.10$ dex) in our solar twin hunting program. Fig. 2 clearly shows that these constrains (in shape of an irregular polygon) do not follow the evolutionary tracks of main sequence stars, thereby introducing a slight bias in mass and removing several solar twin candidates with $M < 1.0\,M_\odot$ in our sample.

In order to address this issue for studies of the Sun's evolution along the main sequence, such as rotational and magnetic evolutionary studies, we propose a new class of star like the Sun[11]: solar proxy stars. Its definition is based on spectroscopic stellar parameter constraints ensuring that the star follows an evolutionary path similar to the Sun on the main sequence. Such constraints are: (1) [Fe/H] and mass values within ±0.15 dex and ±5 per cent of the Sun's, respectively. Stars with these values roughly follow a similar evolutionary path as the Sun; (2) the $\log g$ is only constrained to verify if the star is on the main sequence and its bounds depend on the mass isochrone model (e.g. $\log g$ can takes values from ∼4.1 to 4.6 dex for a solar-mass star); (3) as a result of the above constraints, the T_{eff} takes larger values ranging from ∼5320 to ∼6050 K, none the less to achieve a high precision in stellar parameters we recommend to use T_{eff} values within 150–200 K of the solar value (e.g. to avoid differential 3D and non-LTE effects). All these constraints are very well represented in Fig. 4, where the dashed lines are the evolutionary tracks taken from Yonsei–Yale (Y^2) isochrones (Yi et al. 2001; Demarque et al. 2004) for masses between $0.95\,M_\odot$ and $1.05\,M_\odot$, in steps of 0.05 dex in [Fe/H]. Solar analogue and solar-type stars keep the same definition, i.e. solar analogues are objects with [Fe/H] within a factor of two of solar (Soderblom & King 1998), while solar-type stars are main sequence or subgiant stars with 5000 K < T_{eff} < 6500 K or spectral type ranging from F8V to K2V as is defined in the literature (e.g. see Soderblom & King 1998; Adibekyan et al. 2017).

Applying the above definitions in our sample, we identified 70 solar proxies (from which 42 are solar twins according to the definition of Ramírez et al. 2014), 46 solar analogues, and 13 solar-type stars, which are represented by circles (solar twins and proxies),

diamonds, and squares, respectively in Fig. 4. It is important to mention that we consider as solar twin/proxy/analogue star to those whose uncertainties in fundamental parameters fall into our definition criteria, since our precision is limited by the resolving power. In addition, there are 23 wide binaries (Tokovinin 2014a, b) from which 14 are solar proxies, seven are solar analogues and two are solar-type stars. The spectra of these binaries are not contaminated by their companions. We also identified four new spectroscopic binaries which are not analysed in this work, however they are summarized in Table A4. Despite some stars of our sample have been already analysed by other authors, their stellar parameters were estimated using methods that are different from ours, and with lower SNR or resolving power, or different spectral coverage. In order to identify the closest solar twin in our sample, we have narrowed down the [Fe/H], T_{eff}, $\log g$, and mass to be within of 0.05 dex, 50 K, 0.05 dex, and 0.03 $M_\odot$ of the solar values. As a result, nine stars (HIP 49580, HIP 20218, HIP 11253, HIP 7244, HD 105590A, HD 49425, HD 22875, HD 9201, TYC 1678-109-1) met these strict criteria, whose solar masses and [Fe/H] make them useful for obtaining precise chemical abundances differentially to the Sun. These few objects represent 7 per cent from the total of stars analysed in this work, thus showing how hard they are to find.

4.3 Age and mass

Isochronal mass and age determinations helped us to better understand the evolution of stars, calibrate age correlations as gyrochronology and magnetic activity evolution, as well as to understand the Chemical Evolution of the Galaxy. However, this method relies on isochrones of stellar evolution models and input stellar parameters (T_{eff}, absolute magnitude (M_V) and [Fe/H]) (e.g. Lachaume et al. 1999; Takeda et al. 2007) that usually give large uncertainties (∼3–4 Gyr), biases, or sometimes serious spurious age results because the M_V is generally estimated from photometry of moderate precision. In order to increase the precision in the method, Ramírez et al. (2013, 2014) replaced the M_V by the spectroscopic $\log g$. Using the q^2 code, that performs probability distribution functions of ages and masses from the Y^2 isochrones, these authors not only were able to achieve precise age values, but also greatly reduce their uncertainties to ∼1–2 Gyr (e.g. see the compelling example of HIP 56948 in Meléndez et al. 2012). Spina et al. (2018) improved the q^2 interpolation method by including α-enhancements, spectroscopic $\log g$, and M_V (estimated through *Hipparcos/Gaia*

---

[11]Historically there are three classes of stars like the Sun: solar twins, solar analogue stars, and solar-type stars (Cayrel de Strobel 1996).
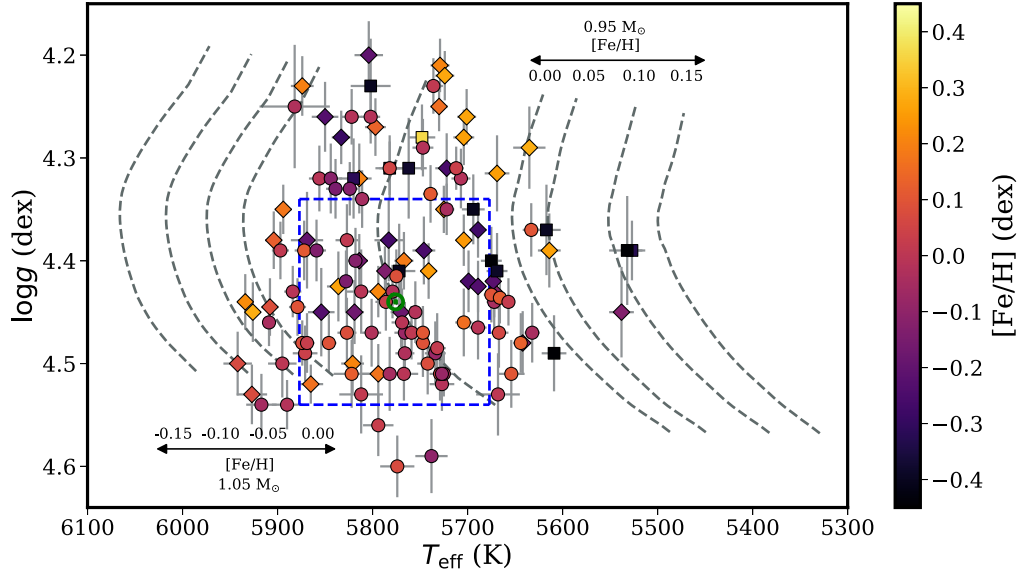
Figure 4. Hertzsprung–Russell diagram plotted using the evolutionary tracks of Y^2 (Yi et al. 2001; Demarque et al. 2004). The left dashed lines represent the evolutionary tracks for 1.05 $M_\odot$ with [Fe/H] from 0.00 to −0.15 dex, while the right dashed lines for 0.95 $M_\odot$ with [Fe/H] from 0.00 to 0.15 dex. The new solar twins and solar proxies are plotted as circles. To differentiate solar twins from solar proxies we also plotted the Ramirez's solar twin definition in blue dashed lines, i.e. all the circles plus their error bars that fall within this region are considered as solar twins. The solar analogues and the solar-type stars are shown in diamonds and squares, respectively. The colourmap represents the [Fe/H] for all the stars. The Sun's data are plotted as reference (green solar standard symbol) with its evolutionary track (i.e. dashed line for 1.0 $M_\odot$ and [Fe/H] = 0.0 dex).

parallaxes) as input parameters (see their equation 3). As a result, these authors further reduce the uncertainties to ∼1.0 Gyr (∼0.5 Gyr using *Gaia* DR2 parallaxes). Despite the improvements performed by Ramírez et al. (2014) and Spina et al. (2018) to the isochronal age estimator, there is still a strong dependence on the precision of the spectroscopic log g which at the same time is sensitive to EWs measurements and therefore also to the ionization balance.

In this work, we estimate isochronal ages using both the improved q^2 and the Bayesian inference. The improved q^2 uses stellar parameters, parallaxes, and Johnson V magnitudes as input parameters. In our age estimations we use the precise *Gaia* EDR3 parallaxes, which are corrected by subtracting −15 ± 18 µas as suggested by Stassun & Torres (2021). Besides, as the Johnson V is not as precise as *Gaia* G, we used the V_G (estimated from equation (2) and with $\sigma(V_G) \sim 0.015$) when the uncertainties of Johnson V are greater than 0.015. It helps us to improve the q2 age estimations and it is also useful when Johnson V is not available. We found a dispersion of only ∼0.04 Gyr between the q2 ages estimated using Johnson V and V_G. On the other hand, the Bayesian inference method (Grieves et al. 2018) employs the Y^2 evolutionary tracks adopting steps of 0.01 M/$M_\odot$ in mass, 0.05 dex in metallicity, and 0.05 dex in [α/Fe]. Posterior distributions of ages and other evolutionary parameters are estimated through the proper marginalization of the likelihood as a function of T_{eff}, [Fe/H],[12] log g, *Gaia* EDR3 parallaxes (already offset by −15 µas) and *Gaia* DR2 G band photometry. We emphasize that we did not use *Gaia* EDR3 G band in the Bayesian method as there are not yet bolometric corrections (BC) for it. For the brightest stars ($G < 6$ mag), we corrected the *Gaia* DR2 G band systematics and applied the BC of Casagrande & VandenBerg (2018) to estimate luminosities. The resulting photometric errors are composed by the quadratic propagation of the nominal G band errors reported

by *Gaia* DR2 and a conservative lower limit of 0.01 mag. The likelihood function is evaluated along each possible evolutionary step (within ±10σ of the input parameter space) and simultaneously weighted by metallicity and mass inputs, which are based on the solar neighbourhood metallicity distribution (Casagrande 2018) and Salpeter initial mass function, respectively. The values adopted for each one of the evolutionary parameters result from the median (50 per cent percentile) and ±1σ intervals (16–84 per cent percentile) yielded by its posterior cumulative distributions.

The left-hand panel of Fig. 5 shows the q^2 ages estimated for our sample using spectroscopic stellar parameters and parallaxes as input parameters (hereafter log g & plx) versus the Bayesian inference ages. There is a good agreement between methods with a dispersion of only ∼0.48 Gyr. This dispersion is estimated removing the most prominent outlier, which is a star with [Fe/H]= −0.5 dex and $M = 0.85$ $M_\odot$. In the middle panel of Fig. 5, we compare the masses and it is shows good agreement with a dispersion of only 0.01 $M_\odot$. As the spectroscopic log g is a fundamental observable for estimating isochronal ages, it is important to make a comparison with the trigonometric gravity. It is estimated from the luminosity ($\propto R^2 T_{eff}^4$) and gravity ($\propto M/R^2$) relations to arrive to the following expression:

$$\log g(\text{Trig}) = \log\left(\frac{M}{M_\odot}\right) + 4\log\left(\frac{T_{eff}}{T_\odot}\right) + 0.4V + 0.4\text{BC}$$
$$+ 2\log\left(\frac{\text{plx}}{1000}\right) + 0.104, \qquad (3)$$

where V is the unreddened visual magnitude, plx the parallax in milliarcsecond, and BC the bolometric correction. The latter is taken from Meléndez et al. (2006). The last term of equation (3) is somewhat different from the literature (e.g. Nissen, Hoeg & Schuster 1997) because we adopted a slightly different absolute bolometric magnitude value for the Sun ($M_{\text{bol},\odot}$ = 4.74; Bessell, Castelli & Plez 1998). As can be seen in the right-hand panel of Fig. 5, there is generally good agreement between the spectroscopic and

---

[12]In this work, we adopted [α/Fe] = 0 as we did not determine the abundance of α-enhancement elements.
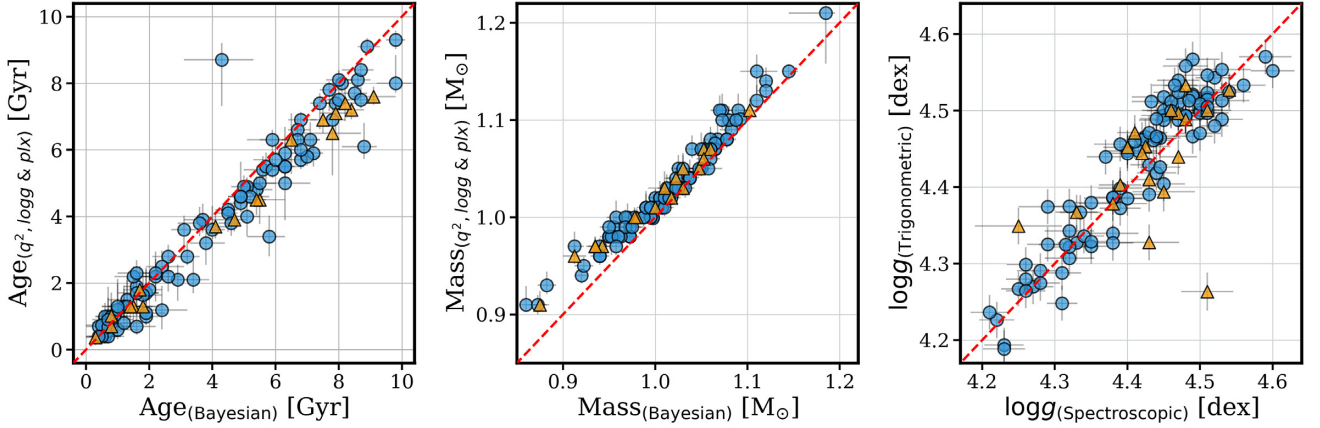
Figure 5. Left-hand panel: Comparison between the q^2 ages estimated using $\log g$ and parallaxes as input parameters versus the Bayesian ages. The latter includes *Gaia* DR2 *G* magnitudes in its calculations. Middle panel: q^2 ($\log g$ and parallaxes) masses versus Bayesian masses. Right-hand panel: Comparison between the spectroscopic and the trigonometric $\log g$ (equation 3). In all panels, the dashed red lines represent the 1:1 ratio, while the yellow triangles the binary stars.

trigonometric $\log g$ (almost within 2σ) with a dispersion of 0.035 dex. Binary stars (represented by yellow triangles) are not considered into the dispersion estimation in all panels of Fig. 5. Therefore, with the above results, we can conclude that the ages determined using q^2 are as precise as those from the Bayesian inference. This is somewhat expected since the errors derived in this work are small enough to reduce the importance of the prior probability assumptions present in Bayesian models. However, particular attention is paid in this point because age determination techniques must be also tested with other methods as for instance gyrochronology, asteroseismology, chemical clocks, etc. In this paper, we adopted the ages estimated using the q^2 since it is shown that this method gives reliable ages as the Bayesian inference. Therefore, the q^2 ages will be used in the figures of the next sections. All our age, mass, and radius results using both methods are summarized in Table A2.

5 STELLAR ROTATION WITH KEPLER & TESS

It is well-known that late-type stars inherit part of the original molecular cloud angular momentum as they are born. Therefore, a large spread in their initial rotational velocities is observed among young open cluster and stellar associations (Bouvier, Forestini & Allain 1997). As the stars arrive at the main sequence, it is expected that magnetized stellar winds, powered by stellar dynamo, drive the angular momentum evolution throughout their evolutionary history, gradually forgetting the initial rotational conditions. Therefore, after a given age, late-type stars tend to converge into well-behaved rotational sequence as a function of mass and age, enabling the calibration of empirical rotation–age-mass relations (Skumanich 1972; Barnes 2003). This age-dating technique is known as gyrochronology and establish a precise rotational clock where stellar ages are estimated from rotational period measurements (Barnes 2003; Meibom et al. 2011, 2015).

In the last decade, a new era for astronomy began with the successful *Kepler* (Borucki et al. 2010), K2 (Howell et al. 2014), and *TESS* (Ricker et al. 2015) missions. In this paper, we take advantage of the large public data base of these surveys to measure rotation periods (P_{rot}) for our sample. We found 31 precise light curves (one in *Kepler*, two in K2, and 28 in *TESS*) where several of them belong to the short and long cadence (e.g. 2 and 30-min cadence observation in *TESS*). To extract *TESS* and Kepler light curves, we repeated the same

procedure adopted in Lorenzo-Oliveira et al. (2020). The light curves were obtained from target pixel files using pixel level decorrelation technique through the LIGHTKURVE[13] python package (Lightkurve Collaboration 2018). For each target, we remove surrounding pixels eventually contaminated by nearby stars. The resulting light curves are cleaned from outliers beyond $\pm 3\sigma$ and in some cases binned in steps of 0.5 h to enhance the signal-to-noise ratio and also mitigate short-term variability (e.g. oscillations, spacecraft pointing jitter).

P_{rot} were initially measured through Generalized Lomb–Scargle analysis. Since most of our stars shows moderate to low level of activity, we restricted our search for rotational periods within a reasonable window between 1 and 50 d. Detected rotation periods are defined by signals in the periodograms with false alarm probability below 1 per cent. In the cases where aliases of the strongest detection are also present and statistically significant, we choose to report the secondary detection together with the strongest one. For a sanity test, the P_{rot} were also estimated through Gaussian Process (GP) that uses a kernel developed from a mixture of two harmonic oscillators (for a complete description see Foreman-Mackey et al. 2020). Fig. 6 shows the reduced light curve of HIP 17936 with the GP model plotted in black solid line and its 2σ model prediction in red shaded region. The P_{rot} estimated with both methods are in a very good agreement and we use the median of them as the adopted rotational period value (see Table A1).

In Fig. 7 are displayed the rotational evolution of our sample of solar proxies (green circles), solar analogues (blue triangles), and the Sun (green solar standard symbol). The shaded region represents the rotational evolution model with solar metallicity and mass within ± 5 per cent of the Sun. The model is based on the period evolution equation established by Barnes (2010) (see equation 32 therein) that includes the convective turnover time-scale (Table 1, Barnes & Kim 2010). We found a good agreement between the isochronal q^2 ages and the rotational evolution model, almost within the uncertainties.

6 CHROMOSPHERIC ACTIVITY

Thanks to the very good performance of the TS23 spectrograph in the blue part of the spectra, we estimated the activity indices for our
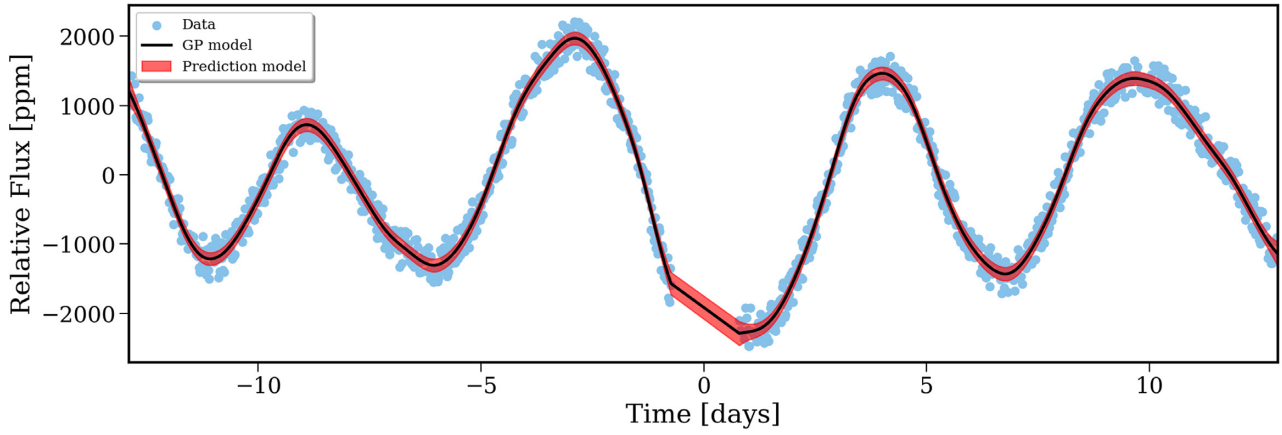
---

[13]https://docs.lightkurve.org/index.html

Figure 6. TESS light curve (filled circles) of the new solar proxy HIP 17936 observed in one sector. The black line represents the GP model, while the red shaded region its 2σ rotation prediction model.
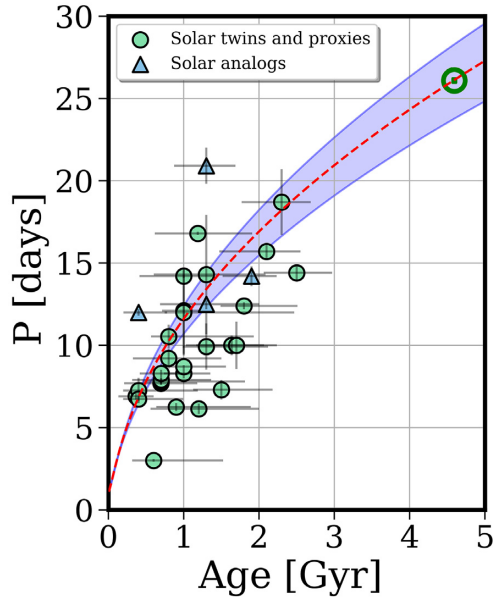

Figure 7. Age–rotation diagram for our solar twins and proxies using model predictions from Barnes (2010) calibrated to the Sun (green solar standard symbol) and with variations of $\pm 0.05\,\mathrm{M_\odot}$ (shaded region). The red dashed line represents the rotational evolution of the Sun.

Figure 8. Mount Wilson system calibration using $S_{\mathrm{HK, TS23}}$ versus $S_{\mathrm{HK, MW}}$. The red dashed line and the blue shaded region represent the linear fit (considering the errors in both axes) and the 95 per cent confidence interval, respectively.

sample by measuring the Ca II H&K emission line fluxes (3933.664 Å and 3968.470 Å). The normalization of the spectral region bracketing the Ca II lines demands a different normalization procedure. In order to ensure the overall consistency of activity measurements, for each star, we performed a differential normalization procedure of the *echelle* spectral orders that surround the Ca II lines. As a template to guide the normalization procedure of a given star, we build a high SNR master spectrum from the large HARPS ($R = 115\,000$) time-series and thus degraded the resolving power to match with TS23 observations ($R = 60\,000$). In the cases where no HARPS observations were performed for a given TS23 solar twin candidate, we choose another HARPS star with similar T_{eff} and [Fe/H] as a template. The S_{HK} index was calculated following the prescription given in Wright et al. (2004). In order to perform a reliable calibration of our $S_{\mathrm{HK, TS23}}$ indices into the Mount Wilson system (MW), we first
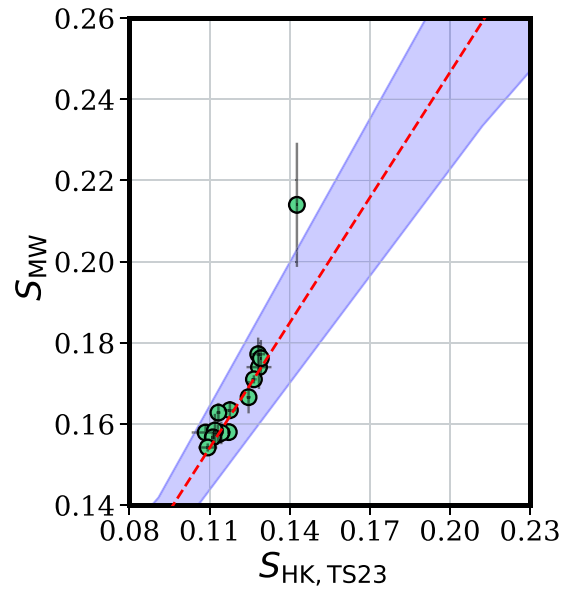
selected a subsample of 10 stars whose S_{MW} are very well estimated by Lorenzo-Oliveira et al. (2018) and then complemented with five new solar-type stars found in the European Southern Observatory (ESO) archive[14] also with common observations between HARPS and TS23. This sample of 15 stars is distributed between active and inactive regimes (Table A3). As a result, we obtain the following calibration equation:

$$S_{\mathrm{MW}} = 0.038(\pm 0.015) + 1.048(\pm 0.125) \times S_{\mathrm{HK, TS23}}, \qquad (4)$$

where the typical standard deviation of the linear fit is 0.0073 (see Fig. 8), comparable with calibrations carried out using spectrographs

[14]http://archive.eso.org/wdb/wdb/adp/phase3_spectral/form?phase3_collection = HARPS
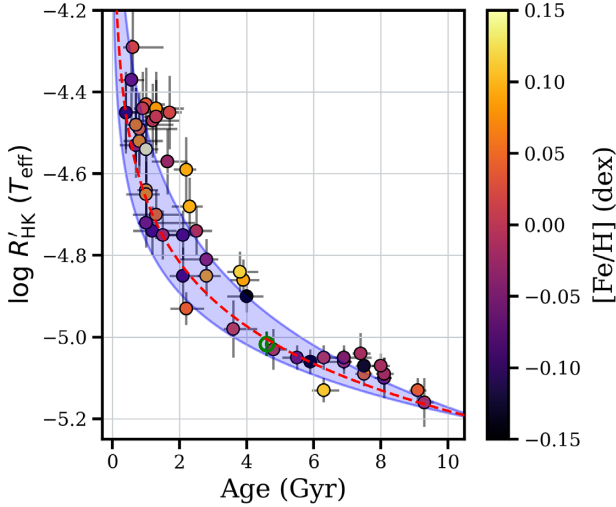
Figure 9. Activity–age diagram for our solar twins and solar proxies. The red dashed line represents the activity–age relation ($R'_{\rm HK}(T_{\rm eff}) \propto {\rm Age}^{-0.52}$) and the shaded region its 2σ activity prediction band found by Lorenzo-Oliveira et al. (2018). The Sun is represented by the green solar standard symbol, while the colourmap shows the metallicity distribution.

of higher resolving power and stability than TS23 (e.g. HARPS). The converted $S_{\rm MW}$ values and their respective errors taking into account photometric and repeatability measurement errors are given in Table A1 for the Inti sample. However, we excluded from our sample stars with $S_{\rm MW}$ values estimated in a single patch epoch.

Activity levels were estimated using log $R'_{\rm HK}(T_{\rm eff})$ index following the procedure given by Lorenzo-Oliveira et al. (2018). We emphasize that log $R'_{\rm HK}(T_{\rm eff})$ should not be confused with the usual log $R'_{\rm HK}$ based on photometric colours (Noyes et al. 1984). For the most active stars, the difference between both indices is negligible, however substantial differences arise after log $R'_{\rm HK} \sim -4.8$ towards the lowest activity levels. Besides, the updated Ca II index log $R'_{\rm HK}(T_{\rm eff})$ shows improved activity–age correlation for inactive stars. To build this index, Lorenzo-Oliveira et al. (2018) removed the photospheric contribution of the $R'_{\rm HK}$ by using an improved photospheric correction as a function of $T_{\rm eff}$ (equation 7 therein) instead of the standard photometric colour $(B - V)$ (Wright et al. 2004). The uncertainties are estimated through random samples from a Gaussian distribution that takes into account the $\sigma(S_{\rm HK, MW})$. As a result, we obtained updated chromospheric indices log $R'_{\rm HK}(T_{\rm eff})$ for our sample and they can be also found in Table A1.

In Fig. 9 are shown the chromospheric indices versus the ages for our solar proxy sample. The activity–age relation found by Lorenzo-Oliveira et al. (2018) is also plotted as red dashed lines with its 2σ activity variability prediction band (shaded region). We can clearly see that our new sample of solar twins/proxies also follows this correlation, thereby favouring the chromospheric activity as a useful clock even for stars older than the Sun. However, notice that the activity–age relation in Lorenzo-Oliveira et al. (2018) was derived using high resolving power ($R = 115\,000$) time-series of Ca II H&K measurements. Besides, the typical [Fe/H] values of their sample are more narrowed around the solar metallicity (± 0.05 dex of the solar value) in comparison to our sample. The latter explains the presence of some outliers in our activity–age diagram. The solar analogue stars and solar-type stars are not included in

Fig. 9 as their mass and [Fe/H] regime are different to the solar proxies.

7 SUMMARY AND CONCLUSIONS

Thanks to the *Gaia* mission, we found a large sample of solar twins candidates through constraints on colour (using Tycho, 2MASS, and *Gaia* EDR3 catalogues) and absolute magnitude (employing *Gaia* EDR3 parallaxes). As our sample is within 100 pc from Earth, reddening corrections are negligible. The definitive colour constraints used for our solar twin hunting program are shown in Table 1 and were established following the spectroscopic solar twin definition given by Ramírez et al. (2014). However, this definition does not consider the evolutionary state of the star, thus introducing a slight bias in the mass distribution in the sample of known solar twins (see Ramírez et al. 2014; Spina et al. 2018). Although the selection criteria of Ramírez et al. (2009) is useful for obtaining precise chemical abundances differentially to the Sun (due to a narrow range in stellar parameters relative to the Sun), that criteria hampers studies dedicated to understand the rotational and magnetic evolution of the Sun. To address this issue for future works, we propose a new class of star like the Sun: solar proxy, whose definition is based not only on stellar parameters constraints, but also on its evolutionary track during the main sequence. In this new definition, the metallicity and the mass define whether a star is a solar proxy or not. These parameters are constrained to be within ± 0.15 dex and 5 per cent to the solar values, thereby assuring that the star follows a similar evolution as the Sun. The log g is assumed to be from ~ 4.1 to 4.6 dex since this constraint is used only to verify if the star is on the main sequence. As is shown in Fig. 4, the $T_{\rm eff}$ of solar proxies can take values ranging from ~ 5310–6050 K, however, for precise abundances, it is recommended to work with stars with $T_{\rm eff}$ within 150–200 K of the solar value in order to avoid 3D and non-LTE effects. Note that the solar proxy limits are not defined by an irregular polygon region, but instead by evolutionary tracks.

Applying all the definitions discussed above, we identified 70 solar proxies, 46 solar analogues, and 13 solar-like stars. Their stellar parameters were estimated through the differential analysis and the spectroscopic equilibrium technique. As a result, we obtained a high internal precision ($\sigma(T_{\rm eff}) = 15$ K, $\sigma(\log g) = 0.03$ dex, $\sigma({\rm [Fe/H]}) = 0.01$ dex, and $\sigma(v_t) = 0.03$ km s^{-1}). We also search the close solar twin within our Inti sample by narrowing down the mass, $T_{\rm eff}$, log g, and [Fe/H] values to 0.03 $M_\odot$, 50 K, 0.05 dex, and 0.05 dex relative to the solar values, respectively. We found nine potential candidates that meet these rigorous criteria. However, further studies should be performed to confirm these stars as close solar twins (e.g. chemical composition, Li abundances, etc.).

Isochronal ages were estimated trough the Yonsei-Yale ischrones models (Yi et al. 2001) and employing two algorithms that use spectroscopic stellar parameters and precise *Gaia* EDR3 parallaxes as input parameters. The ages and masses show a good agreement between the methods within the uncertainties. We also estimated the trigonometric gravity to compare with the spectroscopic gravity and we found relatively good agreement between them, thus validating our age results. However, this is not the case for some binary stars, and it is necessary to use other age determinations such as gyrochronology, asteroseismology, chromospheric–age relations, etc., in order to evaluate the reliability of the results. We also determine a precise Mount Wilson system calibration for the activity indices ($S_{\rm HK, TS23}$) taken with the TS23 spectrograph at McDonald Observatory (see equation 4 and Fig. 8). With this new calibra-

tion, we obtained improved chromospheric indices (log $R'_{HK}(T_{eff})$; Lorenzo-Oliveira et al. 2018). Our new sample of solar twins/proxies also follow the activity–age correlation, thereby reinforcing the scenario where stars older than the Sun continue to decrease their chromospheric activity (see Fig. 9). Rotational periods were estimated using precise *TESS*, *Kepler*, and K2 light curves after applying the Generalized Lomb–Scargle and Gaussian Process methods.

In this work, we provide to the community precise stellar parameters, ages, chromospheric indices, and rotational periods (albeit we were not able to detect rotational periods in stars older than the Sun; Fig. 7). Finally, the 𝕀nti survey is ideal for exoplanet searches around stars like the Sun (e.g. Bedell et al. 2015), in the quest for Solar System analogues.

DATA AVAILABILITY

The 𝕀nti survey is available through MNRAS in its online supplementary material, and its spectra can be shared on request to the corresponding author.

NOTE ADDED IN PROOF

We noted that the star HIP 48443 (TIC 4897275) has been reported as a possible planet host based on TESS observations (see https: //exo.mast.stsci.edu/). The precision parameters given in this work can improve the reported planet properties.

REFERENCES

Adibekyan V. Z., González Hernández J. I., Delgado Mena E., Sousa S. G., Santos N. C., Israelian G., Figueira P., Bertran de Lis S., 2014, A&A, 564, L15
Adibekyan V. et al., 2017, Astron. Nachr., 338, 442
Barnes S. A., 2003, ApJ, 586, 464
Barnes S. A., 2010, ApJ, 722, 222
Barnes S. A., Kim Y.-C., 2010, ApJ, 721, 675
Baumann P., Ramírez I., Meléndez J., Asplund M., Lind K., 2010, A&A, 519, A87
Bazot M. et al., 2012, A&A, 544, A106
Bazot M., Creevey O., Christensen-Dalsgaard J., Meléndez J., 2018, A&A, 619, A172
Bedell M., Meléndez J., Bean J. L., Ramírez I., Leite P., Asplund M., 2014, ApJ, 795, 23
Bedell M. et al., 2015, A&A, 581, A34
Bedell M. et al., 2017, ApJ, 839, 94
Bedell M. et al., 2018, ApJ, 865, 68
Bessell M. S., Castelli F., Plez B., 1998, A&A, 333, 231
Blanco-Cuaresma S., 2019, MNRAS, 486, 2075
Blanco-Cuaresma S., Soubiran C., Heiter U., Jofré P., 2014, A&A, 569, A111
Boeche C., Grebel E. K., 2016, A&A, 587, A2
Borucki W. J. et al., 2010, Science, 327, 977
Botelho R. B. et al., 2019, MNRAS, 482, 1690
Botelho R. B., Milone A. d. C., Meléndez J., Alves-Brito A., Spina L., Bean J. L., 2020, MNRAS, 499, 2196
Bouvier J., Forestini M., Allain S., 1997, A&A, 326, 1023
Brahm R., Jordán A., Espinoza N., 2017, PASP, 129, 034002
Carlos M., Nissen P. E., Meléndez J., 2016, A&A, 587, A100
Carlos M. et al., 2019, MNRAS, 485, 4052
Casagrande L., 2018, in Recio-Blanco A., de Laverny P., Brown A. G. A., Prusti T., eds, Proc. IAU Symp. 330, Astrometry and Astrophysics in the Gaia Sky. Cambridge University Press, Cambridge, p. 206
Casagrande L., VandenBerg D. A., 2018, MNRAS, 479, L102
Casagrande L., Ramírez I., Meléndez J., Bessell M., Asplund M., 2010, A&A, 512, A54
Casagrande L. et al., 2020, preprint (arXiv:2011.02517)
Castelli F., , Kurucz R. L., 2003, in Piskunov N., Weiss W. W., Gray D. F., eds, Proc. IAU Symp. 210, Modelling of Stellar Atmospheres, Cambridge University Press, Cambridge, p. A20
Cayrel de Strobel G., 1996, A&AR, 7, 243
Cayrel de Strobel G., Bentolila C., 1989, A&A, 211, 324
Cayrel de Strobel G., Knowles N., Hernandez G., Bentolila C., 1981, A&A, 94, 1
Chaplin W. J. et al., 2011, Science, 332, 213
Clemens J. C., Crain J. A., Anderson R., 2004, in Moorwood A. F. M., Iye M., eds, Proc. SPIE Conf. Ser. Vol. 5492, Ground-based Instrumentation for Astronomy. SPIE , Bellingham, p. 331
Cowley C. R., Bord D. J., Yüce K., 2020, Res. Notes Am. Astron. Soc., 4, 106
da Silva R., Porto de Mello G. F., Milone A. C., da Silva L., Ribeiro L. S., Rocha-Pinto H. J., 2012, A&A, 542, A84
Datson J., Flynn C., Portinari L., 2012, MNRAS, 426, 484
Datson J., Flynn C., Portinari L., 2014, MNRAS, 439, 1028
Datson J., Flynn C., Portinari L., 2015, A&A, 574, A124
Demarque P., Woo J.-H., Kim Y.-C., Yi S. K., 2004, ApJS, 155, 667
do Nascimento J. D. J., Takeda Y., Meléndez J., da Costa J. S., Porto de Mello G. F., Castro M., 2013, ApJ, 771, L31
do Nascimento J. D. J. et al., 2020, ApJ, 898, 173
Feltzing S., Howes L. M., McMillan P. J., Stonkutė E., 2017, MNRAS, 465, L109

Flores M., González J. F., Jaque Arancibia M., Saffe C., Buccino A., López F. M., Ibañez Bustos R. V., Miquelarena P., 2018, A&A, 620, A34

Foreman-Mackey D., Luger R., Czekala I., Agol E., Price-Whelan A., Brandt T. D., Barclay T., Bouma L., 2020, exoplanet-dev/exoplanet v0.4.0. Available at: https://doi.org/10.5281/zenodo.1998447

Friel E., Cayrel de Strobel G., Chmielewski Y., Spite M., Lebre A., Bentolila C., 1993, A&A, 274, 825

Gaia Collaboration, 2018, A&A, 616, A1

Gaia Collaboration, Brown A. G. A., Vallenari A., Prusti T., de Bruijne J. H. J., Babusiaux C., Biermann M., 2020, preprint (arXiv:2012.01533)

Galarza J. Y., Meléndez J., Cohen J. G., 2016, A&A, 589, A65

Galeev A. I., Bikmaev I. F., Musaev F. A., Galazutdinov G. A., 2004, Astron. Rep., 48, 492

Ginsburg A. et al., 2019, AJ, 157, 98

Giribaldi R. E., Porto de Mello G. F., Lorenzo-Oliveira D., Amôres E. B., Ubaldo-Melo M. L., 2019, A&A, 629, A33

González Hernández J. I., Israelian G., Santos N. C., Sousa S., Delgado-Mena E., Neves V., Udry S., 2010, ApJ, 720, 1592

González Hernández J. I., Delgado-Mena E., Sousa S. G., Israelian G., Santos N. C., Adibekyan V. Z., Udry S., 2013, A&A, 552, A6

Green G. M., Schlafly E., Zucker C., Speagle J. S., Finkbeiner D., 2019, ApJ, 887, 93

Grieves N. et al., 2018, MNRAS, 481, 3244

Hall J. C., Lockwood G. W., Skiff B. A., 2007, AJ, 133, 862

Hall J. C., Henry G. W., Lockwood G. W., Skiff B. A., Saar S. H., 2009, AJ, 138, 312

Hardorp J., 1978, A&A, 63, 383

Holmberg J., Flynn C., Portinari L., 2006, MNRAS, 367, 449

Howell S. B. et al., 2014, PASP, 126, 398

Hunter J. D., 2007, Comput. Sci. Eng., 9, 90

Høg E. et al., 2000, A&A, 355, L27

Jackson H., Jofre P., Yaxley K., Das P., de Brito Silva D., Foley R., 2021, MNRAS, 502, 32

Jasmim F. L., Lazzaro D., Carvano J. M. F., Mothé-Diniz T., Hasselmann P. H., 2013, A&A, 552, A85

Jofré P., Mädler T., Gilmore G., Casey A. R., Soubiran C., Worley C., 2015, MNRAS, 453, 1428

Jofré P., Das P., Bertranpetit J., Foley R., 2017, MNRAS, 467, 1140

Jofré P., Jackson H., Tucci Maia M., 2020, A&A, 633, L9

Kharchenko N. V., 2001, Kinemat. Fizika Nebesnykh Tel, 17, 409

King J. R., Boesgaard A. M., Schuler S. C., 2005, AJ, 130, 2318

Lachaume R., Dominik C., Lanz T., Habing H. J., 1999, A&A, 348, 897

Lallement R., Vergely J. L., Valette B., Puspitarini L., Eyer L., Casagrande L., 2014, A&A, 561, A91

Lazzaro D., Angeli C. A., Carvano J. M., Mothé-Diniz T., Duffard R., Florczak M., 2004, Icarus, 172, 179

Lightkurve Collaboration, 2018, Lightkurve: Kepler and TESS time series analysis in Python, Astrophysics Source Code Library, record ascl:1812.013

Liu F. et al., 2016, MNRAS, 456, 2636

Lorenzo-Oliveira D., Porto de Mello G. F., Schiavon R. P., 2016, A&A, 594, L3

Lorenzo-Oliveira D. et al., 2018, A&A, 619, A73

Lorenzo-Oliveira D. et al., 2019, MNRAS, 485, L68

Lorenzo-Oliveira D., Meléndez J., Ponte G., Galarza J. Y., 2020, MNRAS, 495, L61

Maia M. T., Meléndez J., Lorenzo-Oliveira D., Spina L., Jofré P., 2019, A&A, 628, A126

Maldonado J., Eiroa C., Villaver E., Montesinos B., Mora A., 2015, A&A, 579, A20

Mamajek E. E., Hillenbrand L. A., 2008, ApJ, 687, 1264

Marrese P. M., Marinoni S., Fabrizio M., Giuffrida G., 2017, A&A, 607, A105

McKinney W., 2010, in van der Walt S., Millman J., eds, Proceedings of the 9th Python in Science Conference. p. 51, Available at: https://conference.scipy.org/proceedings/scipy2010/

Meibom S., Mathieu R. D., Stassun K. G., Liebesny P., Saar S. H., 2011, ApJ, 733, 115

Meibom S., Barnes S. A., Platais I., Gilliland R. L., Latham D. W., Mathieu R. D., 2015, Nature, 517, 589

Meléndez J., Ramírez I., 2007, ApJ, 669, L89

Meléndez J., Dodds-Eden K., Robles J. A., 2006, ApJ, 641, L133

Meléndez J., Asplund M., Gustafsson B., Yong D., 2009, ApJ, 704, L66

Meléndez J. et al., 2012, A&A, 543, A29

Meléndez J., Schirbel L., Monroe T. R., Yong D., Ramírez I., Asplund M., 2014a, A&A, 567, L3

Meléndez J. et al., 2014b, ApJ, 791, 14

Meléndez J. et al., 2017, A&A, 597, A34

Nissen P. E., 2015, A&A, 579, A52

Nissen P. E., Hoeg E., Schuster W. J., 1997, in Bonnet R. M. et al., eds, ESA Special Publication, Vol. 402, Hipparcos - Venice '97. p. 225

Nissen P. E., Silva Aguirre V., Christensen-Dalsgaard J., Collet R., Grundahl F., Slumstrup D., 2017, A&A, 608, A112

Nissen P. E., Christensen-Dalsgaard J., Mosumgaard J. R., Silva Aguirre V., Spitoni E., Verma K., 2020, A&A, 640, A81

Noyes R. W., Hartmann L. W., Baliunas S. L., Duncan D. K., Vaughan A. H., 1984, ApJ, 279, 763

Pace G., 2013, A&A, 551, L8

Pasquini L., Biazzo K., Bonifacio P., Randich S., Bedin L. R., 2008, A&A, 489, 677

Porto de Mello G. F., da Silva L., 1997, ApJ, 482, L89

Porto de Mello G. F., da Silva R., da Silva L., de Nader R. V., 2014, A&A, 563, A52

Ramírez I., Meléndez J., Asplund M., 2009, A&A, 508, L17

Ramírez I. et al., 2012, ApJ, 752, 5

Ramírez I., Allende Prieto C., Lambert D. L., 2013, ApJ, 764, 78

Ramírez I. et al., 2014, A&A, 572, A48

Reis W., Corradi W., de Avillez M. A., Santos F. P., 2011, ApJ, 734, 8

Ricker G. R. et al., 2015, J. Astron. Telesc. Instrum. Syst., 1, 014003

Saffe C., Flores M., Miquelarena P., López F. M., Jaque Arancibia M., Collado A., Jofré E., Petrucci R., 2018, A&A, 620, A54

Schuler S. C., Flateau D., Cunha K., King J. R., Ghezzi L., Smith V. V., 2011, ApJ, 732, 55

Science Software Branch at STScI, 2012, PyRAF: Python alternative for IRAF, record ascl:1207.011

Skrutskie M. F. et al., 2006, AJ, 131, 1163

Skumanich A., 1972, ApJ, 171, 565

Sneden C. A., 1973, PhD thesis, The University of Texas at Austin

Soderblom D. R., , King J. R., 1998, in Hall J. C., ed., Solar Analogs: Characteristics and Optimum Candidates, Lowell Observatory, p. 41

Sousa S. G., Santos N. C., Israelian G., Mayor M., Udry S., 2011, A&A, 533, A141

Spina L., Meléndez J., Ramírez I., 2016a, A&A, 585, A152

Spina L., Meléndez J., Karakas A. I., Ramírez I., Monroe T. R., Asplund M., Yong D., 2016b, A&A, 593, A125

Spina L. et al., 2018, MNRAS, 474, 2580

Stassun K. G., Torres G., 2021, ApJ, 907, L33

Takeda Y., Tajitsu A., 2009, PASJ, 61, 471

Takeda Y., Kawanomoto S., Honda S., Ando H., Sakurai T., 2007, A&A, 468, 663

Terlouw J. P., Vogelaar M. G. R., 2015, Kapteyn Package, version 2.3. Kapteyn Astronomical Institute, Groningen

Tody D., 1986, in Crawford D. L., ed., Proc. SPIE, Vol. 627, Instrumentation in Astronomy VI. SPIE, Bellingham, p. 733

Tokovinin A., 2014a, AJ, 147, 86

Tokovinin A., 2014b, AJ, 147, 87

Tucci Maia M., Ramírez I., Meléndez J., Bedell M., Bean J. L., Asplund M., 2016, A&A, 590, A32

Tull R. G., MacQueen P. J., Sneden C., Lambert D. L., 1995, PASP, 107, 251

Unterborn C. T., Johnson J. A., Panero W. R., 2015, ApJ, 806, 139

van der Walt S., Colbert S. C., Varoquaux G., 2011, Comput. Sci. Eng., 13, 22

Vergely J. L., Valette B., Lallement R., Raimond S., 2010, A&A, 518, A31

Wright J. T., Marcy G. W., Butler R. P., Vogt S. S., 2004, ApJS, 152, 261

Yana Galarza J., Meléndez J., Ramírez I., Yong D., Karakas A. I., Asplund M., Liu F., 2016, A&A, 589, A17

Yana Galarza J. et al., 2019, MNRAS, 490, L86

Yana Galarza J., Meléndez J., Karakas A. I., Asplund M., Lorenzo-Oliveira D., 2021, MNRAS, 502, L104

Yi S., Demarque P., Kim Y.-C., Lee Y.-W., Ree C. H., Lejeune T., Barnes S., 2001, ApJS, 136, 417

Önehag A., Korn A., Gustafsson B., Stempels E., Vandenberg D. A., 2011, A&A, 528, A85

SUPPORTING INFORMATION

Supplementary data are available at *MNRAS* online.

Table A1. Stellar parameters for the ℑnti survey.
Table A2. Fundamental parameters for the ℑnti survey.

Please note: Oxford University Press is not responsible for the content or functionality of any supporting materials supplied by the authors. Any queries (other than missing material) should be directed to the corresponding author for the article.

APPENDIX A: TABLES

Table A1. Stellar parameters for the 𝕀𝕟𝕥𝕚 survey. This table is available in its entirety in machine readable format at the CDS.

Gaia EDR3	Identifier	$T_{\rm eff}$ (K)	$\log g$ (dex)	$\log g_{\rm Trigonometric}$ (dex)	[Fe/H] (dex)	v_t (km s^{-1})	$S_{\rm MW}$	$\log R'_{\rm HK}(T_{\rm eff})$	$P_{\rm rot}$	Remarks
2117267079903573504	TYC 3130-2191-1	5722 ± 8	4.350 ± 0.025	4.380 ± 0.023	−0.040 ± 0.007	1.03 ± 0.02	0.161 ± 0.006	−5.10 ± 0.05	–	1
2975480199938221056	HIP 8522	5727 ± 13	4.520 ± 0.026	4.543 ± 0.023	−0.017 ± 0.010	1.11 ± 0.03	0.324 ± 0.003	−4.53 ± 0.08	7.7 ± 0.1	1
4529634417760144896	HD 168069	5871 ± 13	4.490 ± 0.027	4.466 ± 0.023	0.038 ± 0.009	1.05 ± 0.02	0.178 ± 0.003	−4.93 ± 0.04	–	1
1761984258439478784	HIP 103025	5827 ± 12	4.380 ± 0.035	4.339 ± 0.023	0.013 ± 0.008	1.14 ± 0.02	0.161 ± 0.003	−5.05 ± 0.03	–	1
9908441147605158840	HD 49425	5779 ± 9	4.430 ± 0.026	4.429 ± 0.023	−0.026 ± 0.008	1.11 ± 0.02	–	–	–	1
2720269806723503336	HIP 20722	5846 ± 8	4.480 ± 0.028	4.493 ± 0.023	0.092 ± 0.008	1.10 ± 0.02	0.257 ± 0.027	−4.64 ± 0.10	8.3 ± 0.3	1
7407358683268583868	HIP 49580	5801 ± 10	4.470 ± 0.033	4.487 ± 0.023	−0.023 ± 0.009	1.03 ± 0.02	0.210 ± 0.003	−4.81 ± 0.05	–	1
1508557582834745088	HIP 69709	5856 ± 11	4.320 ± 0.032	4.322 ± 0.023	−0.007 ± 0.009	1.14 ± 0.02	0.159 ± 0.003	−5.06 ± 0.03	–	1
3555715878289406208	HIP 52649	5811 ± 11	4.340 ± 0.028	4.336 ± 0.023	−0.046 ± 0.009	1.10 ± 0.02	0.163 ± 0.003	−5.05 ± 0.03	–	1
1260316891261098752	HIP 69230	5734 ± 11	4.490 ± 0.031	4.521 ± 0.023	−0.078 ± 0.009	1.03 ± 0.03	0.238 ± 0.003	−4.74 ± 0.06	16.8 ± 0.1	1
3915429733361853952	HIP 55820	5672 ± 8	4.440 ± 0.027	4.463 ± 0.023	−0.044 ± 0.007	0.98 ± 0.02	0.171 ± 0.003	−5.05 ± 0.03	–	1
2136741591197747712	HD 184424	5827 ± 10	4.470 ± 0.034	4.497 ± 0.023	0.083 ± 0.009	1.19 ± 0.02	0.308 ± 0.009	−4.52 ± 0.08	9.2 ± 0.6	1
3457655518914443968	HIP 9172	5794 ± 16	4.560 ± 0.030	4.533 ± 0.023	0.031 ± 0.013	1.24 ± 0.03	0.367 ± 0.009	−4.43 ± 0.09	8.7 ± 0.1	1
6373290674775530368	HIP 46076	5766 ± 11	4.470 ± 0.030	4.509 ± 0.023	−0.076 ± 0.010	1.05 ± 0.03	0.229 ± 0.005	−4.75 ± 0.06	15.7 ± 0.5	1
3203761005400205824	HIP 20218	5755 ± 9	4.450 ± 0.030	4.500 ± 0.023	−0.015 ± 0.009	1.09 ± 0.02	0.234 ± 0.003	−4.74 ± 0.06	14.4 ± 0.5	1
1323563308352525440	HIP 79068	5874 ± 7	4.480 ± 0.022	4.492 ± 0.023	0.084 ± 0.007	1.09 ± 0.02	0.252 ± 0.016	−4.65 ± 0.08	14.2 ± 0.1	1
8824102780288835584	HIP 38647	5767 ± 15	4.510 ± 0.026	4.517 ± 0.023	−0.006 ± 0.012	1.11 ± 0.03	0.231 ± 0.004	−4.75 ± 0.06	7.3 ± 0.6	1
2917013969223480672	HIP 7244	5766 ± 10	4.490 ± 0.024	4.519 ± 0.023	−0.028 ± 0.009	1.13 ± 0.02	0.298 ± 0.012	−4.57 ± 0.08	10.0 ± 0.6	1
3331060541836616000	HIP 10321	5725 ± 10	4.510 ± 0.022	4.523 ± 0.023	−0.020 ± 0.007	0.97 ± 0.02	0.347 ± 0.006	−4.48 ± 0.09	7.8 ± 0.2	1
4511284594842685544	HD 229450A	5739 ± 8	4.335 ± 0.028	4.367 ± 0.023	0.109 ± 0.009	1.04 ± 0.02	0.156 ± 0.003	−5.13 ± 0.03	–	1
2869747927140286208	HD 221103	5879 ± 9	4.445 ± 0.028	4.426 ± 0.023	0.097 ± 0.008	1.14 ± 0.02	0.194 ± 0.003	−4.85 ± 0.05	–	1
2163433717746084352	TYC 3588-6756-1	5812 ± 23	4.530 ± 0.038	4.513 ± 0.023	0.015 ± 0.017	1.45 ± 0.04	0.464 ± 0.010	−4.29 ± 0.11	3.0 ± 0.1	1
4534307273451743744	HD 342979	5667 ± 10	4.470 ± 0.034	4.524 ± 0.023	0.060 ± 0.009	0.99 ± 0.03	0.259 ± 0.006	−4.70 ± 0.06	14.3 ± 3.6	1
1855968480863250176	HIP 101893	5729 ± 11	4.510 ± 0.026	4.514 ± 0.023	0.058 ± 0.009	1.17 ± 0.02	0.345 ± 0.004	−4.49 ± 0.09	10.5 ± 0.7	1
1909471786118933120	HD 213244	5689 ± 9	4.465 ± 0.031	4.533 ± 0.023	−0.006 ± 0.008	1.09 ± 0.03	0.362 ± 0.008	−4.47 ± 0.09	6.2 ± 0.3	1
2196984318618671360	TYC 4250-1364-1	5747 ± 8	4.480 ± 0.033	4.493 ± 0.023	0.092 ± 0.008	1.12 ± 0.02	0.291 ± 0.007	−4.59 ± 0.08	–	1
1792706331305783808	TYC 1678-109-1	5769 ± 11	4.460 ± 0.033	4.499 ± 0.023	−0.005 ± 0.010	1.18 ± 0.03	–	–	–	1
1962597885872344704	TYC 3210-873-1	5742 ± 11	4.500 ± 0.030	4.508 ± 0.023	0.080 ± 0.010	1.16 ± 0.03	0.370 ± 0.004	−4.44 ± 0.09	9.9 ± 1.4	1
2003130042007448704	HD 235929	5668 ± 23	4.530 ± 0.040	4.553 ± 0.023	0.007 ± 0.015	1.17 ± 0.04	0.385 ± 0.003	−4.44 ± 0.09	6.3 ± 0.3	1
1796825582900925056	TYC 2211-2123-1	5775 ± 9	4.415 ± 0.026	4.447 ± 0.023	0.087 ± 0.008	1.06 ± 0.02	0.199 ± 0.005	−4.86 ± 0.05	–	1
1957736635726467840	TYC 3208-1984-1	5675 ± 8	4.433 ± 0.027	4.512 ± 0.023	0.096 ± 0.007	1.08 ± 0.02	0.265 ± 0.005	−4.68 ± 0.07	18.7 ± 2.0	1
1989930095677359616	HD 235957	5707 ± 10	4.320 ± 0.029	4.375 ± 0.023	−0.020 ± 0.008	1.08 ± 0.02	0.163 ± 0.004	−5.09 ± 0.04	–	1
2250381486672264384	HD 22875	5732 ± 9	4.485 ± 0.034	4.513 ± 0.023	0.018 ± 0.009	1.21 ± 0.03	0.366 ± 0.004	−4.45 ± 0.09	10.0 ± 1.4	1†
1807690750662760576	HD 190340	5872 ± 10	4.390 ± 0.029	4.403 ± 0.023	0.109 ± 0.009	1.12 ± 0.02	0.228 ± 0.003	−4.72 ± 0.06	–	1
2592050460006416832	HD 9201	5786 ± 11	4.440 ± 0.028	4.466 ± 0.023	0.035 ± 0.009	1.06 ± 0.02	–	–	–	1†
1323719615110178856	HIP 11253	5812 ± 15	4.430 ± 0.041	4.328 ± 0.023	−0.006 ± 0.012	1.17 ± 0.03	0.180 ± 0.003	−4.94 ± 0.04	–	1†
1605622057017876992	HIP 71989	5890 ± 16	4.540 ± 0.024	4.527 ± 0.023	−0.016 ± 0.010	1.00 ± 0.03	0.298 ± 0.006	−4.53 ± 0.08	6.9 ± 0.2	1†
2257140386478701568	HIP 91210	5869 ± 8	4.480 ± 0.029	4.488 ± 0.023	0.029 ± 0.008	1.10 ± 0.02	0.244 ± 0.003	−4.67 ± 0.06	–	1†
3827020717791837056	HIP 47312	5884 ± 9	4.430 ± 0.025	4.410 ± 0.023	−0.010 ± 0.007	1.11 ± 0.02	0.172 ± 0.004	−4.96 ± 0.04	–	1†
8555237140362230016	HIP 52278	5727 ± 9	4.510 ± 0.019	4.505 ± 0.023	−0.079 ± 0.006	1.02 ± 0.02	0.208 ± 0.014	−4.85 ± 0.07	–	1†
3574377616021489024	HD 105590A	5759 ± 8	4.470 ± 0.026	4.439 ± 0.023	0.010 ± 0.008	1.03 ± 0.02	0.162 ± 0.003	−5.08 ± 0.03	–	1†
1610658885425227264	HIP 71440	5782 ± 20	4.510 ± 0.036	4.263 ± 0.025	−0.046 ± 0.015	1.17 ± 0.03	0.319 ± 0.004	−4.52 ± 0.08	6.2 ± 0.3	1†

Note. (1) Solar twins, (2) Solar proxies, (3) Solar analogs, (4) Solar-type stars, (†) Binary star.

Table A2. Fundamental parameters for the 'Inti' survey. This table is available in its entirety in machine readable format at the CDS.

Gaia EDR3	Identifier	Age (Gyr) (q² & log g & plx)	Mass (M☉) (q² & log g & plx)	Radius (R☉) (q² & log g & plx)	Age (Gyr) (Bayesian)	Mass (M☉) (Bayesian)	Radius (R☉) (Bayesian)	Remarks
2117267079903573504	TYC 3130-2191-1	8.10 (+0.52)(−0.29)	0.960 (+0.014)(−0.007)	1.060 (+0.014)(−0.008)	8.60 (+0.40)(−0.60)	0.940 (+0.010)(−0.008)	1.045 (+0.010)(−0.013)	1
2975480199382 21056	HIP 8522	0.70 (+0.97)(−0.49)	0.999 (+0.004)(−0.004)	0.902 (+0.004)(−0.004)	0.60 (+0.50)(−0.40)	0.998 (+0.008)(−0.008)	0.893 (+0.008)(−0.010)	1
4529634417760144896	HD 168069	2.20 (+1.01)(−0.48)	1.050 (+0.008)(−0.008)	1.000 (+0.010)(−0.009)	2.20 (+0.50)(−0.60)	1.050 (+0.010)(−0.010)	0.993 (+0.010)(−0.010)	1
1761984258439478784	HIP 103025	6.30 (+0.82)(−0.29)	1.020 (+0.009)(−0.008)	1.130 (+0.009)(−0.009)	7.10 (+0.30)(−0.40)	1.000 (+0.008)(−0.008)	1.123 (+0.010)(−0.010)	1
990844114760515840	HD 49425	5.40 (+1.07)(−0.67)	0.990 (+0.009)(−0.008)	1.010 (+0.007)(−0.009)	5.60 (+0.40)(−0.60)	0.973 (+0.015)(−0.010)	0.998 (+0.008)(−0.008)	1
2720269806723 50336	HIP 20722	1.00 (+0.62)(−0.27)	1.070 (+0.017)(−0.009)	0.980 (+0.016)(−0.008)	0.90 (+0.50)(−0.40)	1.065 (+0.010)(−0.010)	0.973 (+0.010)(−0.008)	1
740735868326858368	HIP 49580	2.80 (+1.14)(−0.79)	1.010 (+0.014)(−0.007)	0.970 (+0.016)(−0.015)	2.60 (+0.70)(−0.50)	1.008 (+0.010)(−0.013)	0.955 (+0.008)(−0.010)	1
1508557582834745088	HIP 69709	6.90 (+0.91)(−0.67)	1.030 (+0.010)(−0.009)	1.180 (+0.016)(−0.023)	6.80 (+0.50)(−0.40)	1.018 (+0.008)(−0.010)	1.160 (+0.010)(−0.010)	1
3557158782894062080	HIP 52649	6.90 (+1.08)(−0.25)	1.000 (+0.008)(−0.009)	1.120 (+0.029)(−0.008)	7.80 (+0.40)(−0.30)	0.978 (+0.008)(−0.008)	1.115 (+0.010)(−0.010)	1
1260316892612 1098752	HIP 69230	1.19 (+1.29)(−0.57)	1.000 (+0.017)(−0.012)	0.900 (+0.008)(−0.007)	2.40 (+0.80)(−0.60)	0.958 (+0.013)(−0.010)	0.893 (+0.010)(−0.010)	1
3915429733361853952	HIP 55820	5.50 (+0.86)(−0.44)	0.960 (+0.016)(−0.009)	0.950 (+0.011)(−0.007)	5.70 (+0.40)(−0.30)	0.940 (+0.008)(−0.008)	0.940 (+0.008)(−0.008)	1
2136741591197747712	HD 184424	0.80 (+1.18)(−0.48)	1.060 (+0.008)(−0.008)	0.970 (+0.009)(−0.008)	0.80 (+0.60)(−0.60)	1.060 (+0.010)(−0.010)	0.965 (+0.010)(−0.010)	1
3457655518914 43968	HIP 9172	1.00 (+0.75)(−0.19)	1.030 (+0.017)(−0.010)	0.930 (+0.011)(−0.007)	0.70 (+0.40)(−0.40)	1.025 (+0.010)(−0.010)	0.920 (+0.010)(−0.008)	1
637329067477530368	HIP 46076	2.10 (+1.08)(−0.63)	1.000 (+0.008)(−0.008)	0.920 (+0.020)(−0.007)	2.90 (+0.70)(−0.90)	0.968 (+0.018)(−0.010)	0.913 (+0.010)(−0.008)	1
3203761005400205824	HIP 20218	2.50 (+0.91)(−0.44)	1.000 (+0.009)(−0.007)	0.940 (+0.008)(−0.008)	2.40 (+0.70)(−0.50)	0.995 (+0.010)(−0.008)	0.935 (+0.010)(−0.010)	1
1323563308352525440	HIP 79068	1.00 (+1.00)(−0.59)	1.080 (+0.014)(−0.008)	0.990 (+0.016)(−0.007)	0.60 (+0.40)(−0.30)	1.078 (+0.008)(−0.010)	0.980 (+0.008)(−0.008)	1
882410278028 83584	HIP 38647	1.50 (+1.05)(−0.37)	1.010 (+0.011)(−0.008)	0.930 (+0.009)(−0.007)	1.30 (+0.70)(−0.60)	1.008 (+0.010)(−0.010)	0.920 (+0.010)(−0.008)	1
2917011396922348672	HIP 7244	1.64 (+1.07)(−0.47)	1.000 (+0.013)(−0.007)	0.920 (+0.012)(−0.007)	1.80 (+0.60)(−0.60)	0.988 (+0.010)(−0.010)	0.925 (+0.008)(−0.010)	1
3331060541836 16000	HIP 10321	0.70 (+1.35)(−0.24)	1.010 (+0.014)(−0.009)	0.910 (+0.009)(−0.007)	1.60 (+0.60)(−0.60)	0.995 (+0.010)(−0.010)	0.910 (+0.008)(−0.010)	1
4511284599484268544	HD 229450A	6.30 (+0.82)(−0.36)	1.020 (+0.007)(−0.008)	1.100 (+0.008)(−0.008)	6.70 (+0.50)(−0.50)	1.005 (+0.008)(−0.010)	1.085 (+0.013)(−0.010)	1
2869747927140286208	HD 221103	2.80 (+0.70)(−0.27)	1.070 (+0.014)(−0.008)	1.050 (+0.008)(−0.008)	3.20 (+0.40)(−0.30)	1.060 (+0.008)(−0.010)	1.045 (+0.008)(−0.010)	1
2163433717746084352	TYC 3588-6756-1	0.60 (+1.21)(−0.29)	1.040 (+0.009)(−0.015)	0.940 (+0.010)(−0.007)	1.00 (+0.80)(−0.60)	1.023 (+0.010)(−0.013)	0.930 (+0.008)(−0.010)	1
4534307273451743744	HD 342979	1.30 (+1.49)(−0.70)	1.000 (+0.011)(−0.008)	0.910 (+0.009)(−0.007)	1.30 (+0.50)(−0.60)	0.995 (+0.010)(−0.010)	0.903 (+0.008)(−0.008)	1
1855968480863250176	HIP 101893	0.80 (+1.36)(−0.24)	1.030 (+0.014)(−0.019)	0.930 (+0.009)(−0.007)	1.20 (+0.60)(−0.60)	1.013 (+0.010)(−0.010)	0.920 (+0.010)(−0.008)	1
1909471786118933120	HD 213244	1.20 (+1.44)(−0.64)	1.000 (+0.008)(−0.009)	0.900 (+0.010)(−0.007)	1.00 (+0.60)(−0.40)	0.988 (+0.008)(−0.010)	0.890 (+0.008)(−0.010)	1
2196984318618671360	TYC 4250-1364-1	2.20 (+0.67)(−0.37)	1.030 (+0.016)(−0.007)	0.970 (+0.014)(−0.010)	1.50 (+0.50)(−0.60)	1.030 (+0.010)(−0.008)	0.948 (+0.010)(−0.010)	1
1792706331305783808	TYC 1678-109-1	2.30 (+1.50)(−0.86)	1.010 (+0.009)(−0.009)	0.950 (+0.016)(−0.009)	2.20 (+0.50)(−0.60)	1.003 (+0.010)(−0.010)	0.935 (+0.010)(−0.010)	1
1962597885872344704	TYC 3210-873-1	1.30 (+1.13)(−0.31)	1.030 (+0.017)(−0.010)	0.940 (+0.009)(−0.007)	1.00 (+0.50)(−0.50)	1.033 (+0.010)(−0.010)	0.935 (+0.010)(−0.008)	1
2003130042007448704	HD 235929	0.90 (+1.26)(−0.26)	0.990 (+0.016)(−0.012)	0.890 (+0.008)(−0.008)	0.70 (+0.80)(−0.50)	0.975 (+0.010)(−0.010)	0.873 (+0.010)(−0.008)	1
1796825582900925056	TYC 2211-2123-1	3.90 (+0.87)(−0.39)	1.030 (+0.014)(−0.009)	1.010 (+0.009)(−0.007)	3.70 (+0.50)(−0.60)	1.025 (+0.008)(−0.010)	1.003 (+0.010)(−0.010)	1
1957736635726467840	TYC 3208-1984-1	2.30 (+0.92)(−0.53)	1.010 (+0.009)(−0.009)	0.940 (+0.014)(−0.008)	1.60 (+0.40)(−0.60)	1.010 (+0.010)(−0.010)	0.923 (+0.008)(−0.010)	1
1989930095677359616	HD 235957	8.10 (+0.53)(−0.25)	0.970 (+0.014)(−0.009)	1.070 (+0.014)(−0.007)	8.00 (+0.50)(−0.40)	0.958 (+0.008)(−0.010)	1.053 (+0.010)(−0.008)	1
2250381486672 64384	HD 22875	1.70 (+1.04)(−0.67)	1.010 (+0.008)(−0.008)	0.920 (+0.009)(−0.007)	1.60 (+0.70)(−0.60)	0.995 (+0.010)(−0.010)	0.913 (+0.010)(−0.008)	1
1807690750662760576	HD 190340	3.70 (+0.75)(−0.36)	1.070 (+0.009)(−0.009)	1.080 (+0.014)(−0.008)	4.10 (+0.40)(−0.50)	1.053 (+0.010)(−0.010)	1.070 (+0.010)(−0.010)	1†
2592050460646 16832	HD 9201	3.60 (+1.06)(−0.65)	1.020 (+0.014)(−0.009)	0.990 (+0.008)(−0.009)	3.10 (+0.60)(−0.40)	1.015 (+0.010)(−0.010)	0.978 (+0.008)(−0.010)	1
1323719611011 7856	HI P11253	6.90 (+0.81)(−0.40)	1.010 (+0.015)(−0.008)	1.130 (+0.018)(−0.014)	7.50 (+0.50)(−0.40)	1.000 (+0.010)(−0.008)	1.153 (+0.020)(−0.018)	1†
1605622057018 76992	HIP 71989	0.37 (+0.47)(−0.23)	1.050 (+0.014)(−0.007)	0.940 (+0.015)(−0.007)	0.30 (+0.40)(−0.30)	1.048 (+0.008)(−0.010)	0.943 (+0.008)(−0.008)	1†
2257140386447 01568	HIP 91210	1.30 (+0.96)(−0.42)	1.060 (+0.015)(−0.009)	0.980 (+0.008)(−0.007)	1.40 (+0.50)(−0.50)	1.053 (+0.010)(−0.008)	0.975 (+0.010)(−0.008)	1†
3827020717791837056	HIP 47312	3.90 (+1.01)(−0.34)	1.040 (+0.009)(−0.010)	1.050 (+0.014)(−0.007)	4.70 (+0.40)(−0.50)	1.023 (+0.008)(−0.010)	1.053 (+0.010)(−0.010)	1†
8555237140362 30016	HIP 52278	2.10 (+0.99)(−0.40)	0.990 (+0.007)(−0.008)	0.910 (+0.010)(−0.007)	3.40 (+0.50)(−0.60)	0.950 (+0.010)(−0.008)	0.903 (+0.010)(−0.010)	1†
3574377616021489024	HD 105590A	4.50 (+1.07)(−0.45)	1.000 (+0.009)(−0.009)	1.000 (+0.015)(−0.009)	5.40 (+0.30)(−0.60)	0.980 (+0.010)(−0.008)	0.995 (+0.010)(−0.008)	1†
1610658885425227264	HIP 71440	7.40 (+1.09)(−0.53)	1.000 (+0.010)(−0.009)	1.150 (+0.020)(−0.031)	8.20 (+0.70)(−0.60)	0.978 (+0.010)(−0.013)	1.138 (+0.033)(−0.028)	1†

Note. (1) Solar twins, (2) Solar proxies, (3) Solar analogs, (4) Solar-type stars, (†) Binary star.

Table A3. Solar twin stars used to calibrated our $S_{HK, TS23}$ indices into the Mount Wilson system (MW).

ID	$S_{HK, TS23}$	$\sigma(S_{HK, TS23})$	S_{MW}	$\sigma(S_{MW})$	Reference
HIP 7585	0.128	0.003	0.177	0.004	($\star$)
HIP 49756	0.118	0.002	0.163	0.002	($\star$)
HIP 79672	0.125	0.001	0.167	0.004	($\star$)
HIP 95962	0.113	0.001	0.163	0.002	($\star$)
HIP 8507	0.129	0.005	0.174	0.005	($\star$)
HIP 77052	0.143	0.000	0.214	0.015	($\star$)
HIP 28066	0.117	0.001	0.158	0.001	($\star$)
HIP 85042	0.112	0.001	0.158	0.004	($\star$)
HIP 118115	0.111	0.001	0.157	0.001	($\star$)
HIP 102040	0.129	0.000	0.176	0.005	($\star$)
HIP 113357	0.109	0.004	0.154	0.001	($\dagger$)
HIP 8102	0.127	0.001	0.171	0.001	($\dagger$)
HIP 1499	0.113	0.002	0.157	0.002	($\dagger$)
HIP 59532	0.109	0.005	0.158	0.002	($\dagger$)
HIP 106006	0.114	0.001	0.158	0.003	($\dagger$)

Note. ($\star$) Lorenzo-Oliveira et al. (2018); ($\dagger$) this work.

Table A4. Spectroscopic binary stars.

Gaia EDR3	Identifier
3985360665753530112	HIP 54191
1438813773578253312	TYC 4202-561-1
2642456024453117056	HD 224033
302429645407269120	TYC 1762-1034-1

This paper has been typeset from a TEX/LATEX file prepared by the author.